# Supplementary Material

# Programmable thermocapillary shaping of thin liquid films

Ran Eshel[1], Valeri Frumkin[1,§], Matan Nice[1], Omer Luria[1], Boris Ferdman[2,3], Nadav Opatovski[2], Khaled Gommed[1], Maxim Shusteff[4], Yoav Shechtman[2,3], and Moran Bercovici[1,2,3,*]

[1] Faculty of Mechanical Engineering, Technion - Israel Institute of Technology, Haifa, 3200003 Israel

[2] Department of Biomedical Engineering, Technion - Israel Institute of Technology, Haifa, 3200003 Israel

[3] Russell Berrie Nanotechnology Institute, Technion - Israel Institute of Technology, Haifa, 3200003 Israel

[4] Lawrence Livermore National Laboratory, 7000 East Ave, Livermore, CA 94550, USA

[§] Current affiliation: Department of Mathematics, Massachusetts Institute of Technology, Cambridge, MA, 02139, United States

## Table of Contents

## S.1. Additional experimental data

### Characterization

Figure S1 provides a characterization of the local deformation induced by the projection of an isolated circular spot, as a function of the projection intensity, and for several different geometric configurations of the metallic pads. In all cases, the system was allowed to achieve a steady state, at which point the polymer film was solidified and its surface was measured using a digital holographic microscope (DHM) [1]. Figure S1 presents a cross-section of the resulting axisymmetric film deformation, relative to an initial film thickness of 60 μm, as a function of the illumination intensity. Here, the diameter of the illumination spot is 500 μm, and the absorbing metal pad array consists of 20 x 20 $\mu$m pads with an edge-to-edge distance of 80 μm. As expected, the magnitude of the resulting deformation is proportional to the illumination intensity, and this correlation is linear with a maximum deformation of approximately 1.2 μm, as shown in the inset. The width of the deformation also increases with intensity, yet more moderately, from ~0.6 mm to ~0.8 mm. Further increase in deformation magnitude can be achieved by increasing the pad array density. Figure S1b shows the resulting deformation as a function of the spacing between the absorbing metal array pads, for the same spot size at a fixed (maximum) projection intensity. The results show that a higher pad density leads to absorbance of a larger fraction of light, resulting in increased heating and larger deformation. The inset shows a linear correlation between the area fraction of the surface covered with metal pads and the deformation magnitude, reaching a maximum of approximately 3 $\mu$m. Interestingly, the width of the deformation over this range remains nearly constant. Figure S1c provides information on the repeatability of the resulting deformation by projecting the same spot size and intensity in three independent experiments using the maximum intensity of the light source. Figure S1d presents an isometric view and cross-sections of the resulting deformation for a 500 μm spot size. As expected, for a circular spot, the resulting deformation is axisymmetric.

Figure S2 presents the deformation due to projection of an annulus pattern, with a linear increase in projection intensity along its azimuth, providing a characterization of the achievable deformation resolution. Figure S2a presents the solidified polymer topography as measured by the DHM. Figure S2b presents the projection intensity (blue line) and the resulting deformation magnitude (red circles), along the azimuthal coordinate along path indicated by the red dashed circle in Figure S2a. We find that the deformation correlates well with the light intensity, and the deformation is able to follow a discontinuity in the in the light intensity with a slope of 5.41 μm/mm. Figure S2c presents the cross sections of the deformation at the azimuthal coordinates indicated by corresponding gray lines in Figure S2a. The green squares in Figure S2b show the average over the full width at half maximum (FWHM) of these deformation profiles as a function of the azimuthal coordinate. The direct dependence of the width on the intensity is shown in Figure S3d.

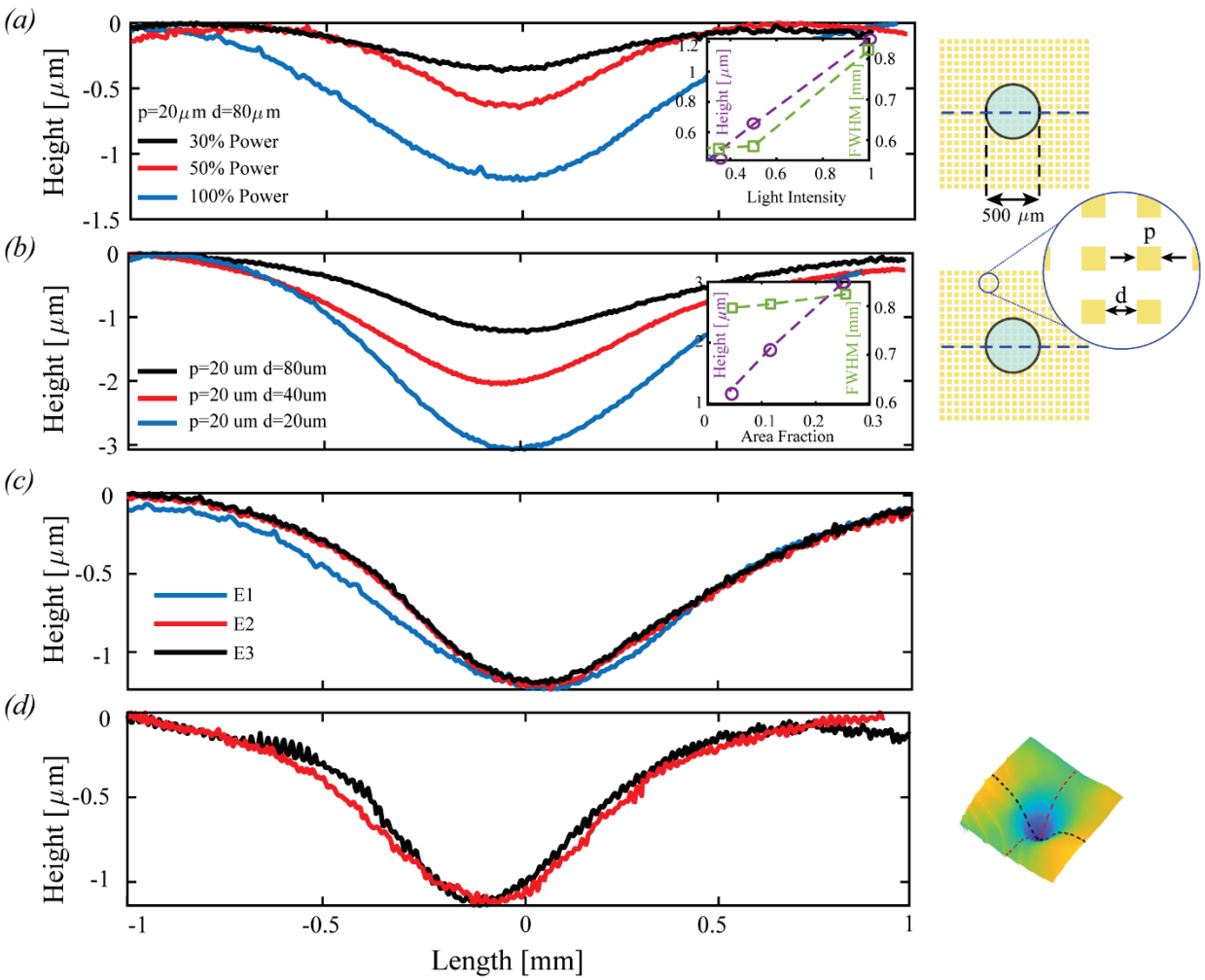


***Figure S1 | Experimental characterization of the deformation magnitude and shape.*** ***(a)*** *A cross-section of the deformation along the horizontal axis (as indicated by the dashed blue line) as a function of the illumination intensity, for a fix pad geometry (p = 20 μm, d = 80 μm). As shown in the inset, the deformation magnitude increases linearly with the illumination intensity. The width of the deformation shows a moderate increase between 50% and 100% intensity.* ***(b)*** *A cross section of the deformation along the horizontal axis as a function of the edge-to-edge distance between pads (d=20,40,80 μm), for a fixed illumination intensity (100%) and a fixed pad size (p x p = 20 x 20 μm). As the gap decreases, a larger fraction of the light per unit area is absorbed, allowing further increase in deformation magnitude. Under these conditions, the width of the deformation is essentially unaffected by the gap size.* ***(c)*** *A cross section of the deformation for three repeats at the same intensity.* ***(d)*** *A horizontal and vertical cross section of the deformation, showing good agreement. All the results in the figure were obtained using a 60 μm film thickness and a 500 μm diameter disk-shaped projection.*

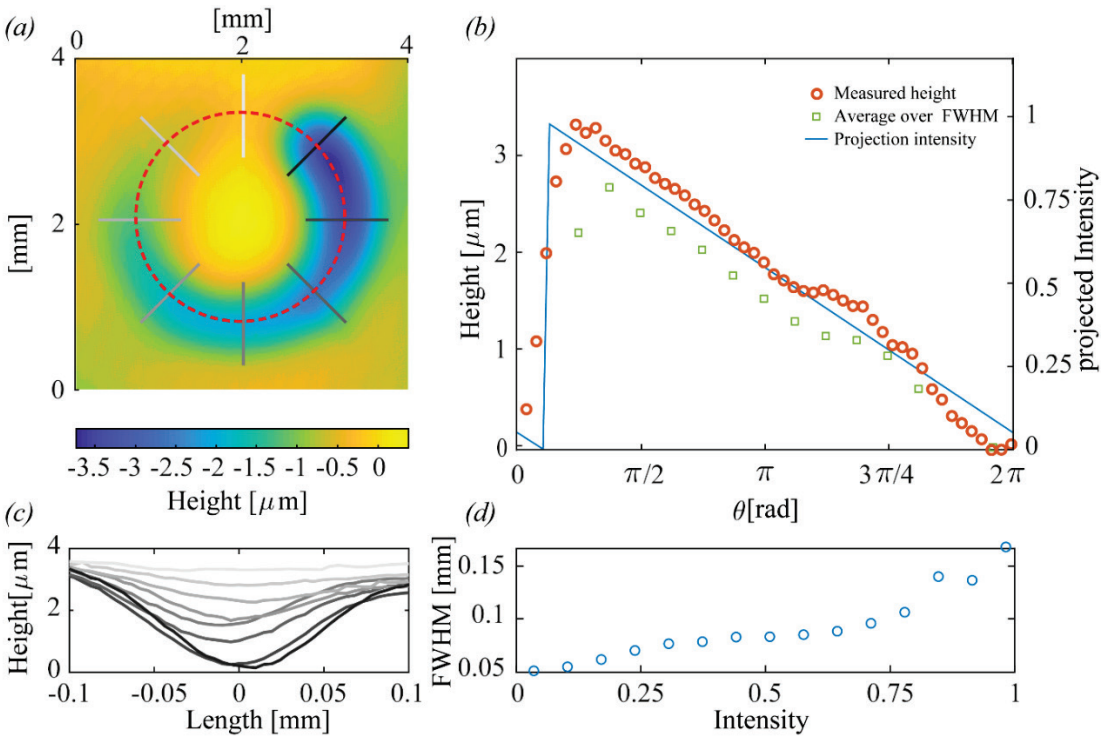


***Figure S2 | Characterization of deformation resolution as a function of projection intensity***. ***(a)*** *Experimental result showing the spatial deformation resulting from projection of an annulus of width 200 µm with an azimuthally varying intensity from 0 to 100%.* ***(b)*** *The magnitude of the deformation (red circles) and the width (FWHM, green squares) at each azimuthal coordinate, together with the projection intensity (blue line) along the centerline of the annulus (red dashed line in* ***a****).* ***(c)*** *Radial cross-sections of the deformation at different azimuthal locations as indicated by corresponding grayscale lines in* ***a****.* ***(d)*** *Full width at half maximum of the deformation as a function of intensity along the annulus pattern.*

## Surface roughness measurements

Figure S3 presents a representative atomic force microscopy (AFM) measurement that we performed over an area of 2.2 x 2.2 µm in order to evaluate the surface roughness of the solidified polymer surface. The resulting topography shows a surface roughness of less than 1 nm RMS over the measured area, which is excellent for nearly all optical applications.

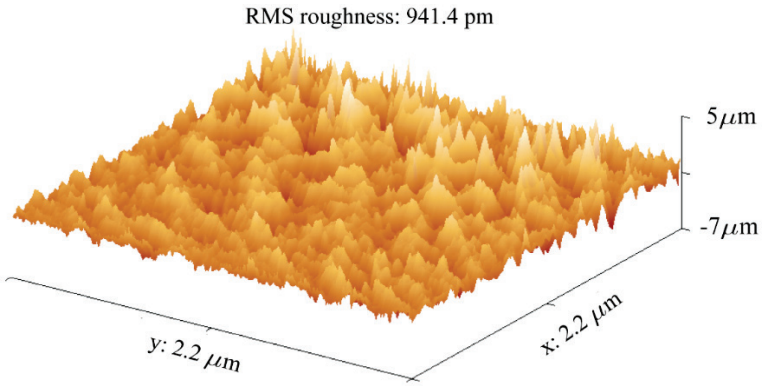


***Figure S3 | AFM measurement of the surface of the solidified polymer.*** *The RMS of the surface roughness is less than 1 nm.*

## S.2. Solutions to the inverse problem

The differential equation describing the steady state deformation of a thin liquid film subjected to a non-uniform temperature gradient is given by (see Appendix A for detailed derivation)

$$\boldsymbol{\nabla}\cdot\left[\frac{S}{3}H^3\vec{\nabla}\nabla^2H-\frac{G}{3}H^3\vec{\nabla}H-\frac{1}{2}H^2\vec{\nabla}\left(\frac{\vartheta_b+\Theta}{1+BH}\right)\right]=0. \tag{S1}$$

The ansatz for the the two-dimensional inverse problem is given by

$$\vartheta_b=\frac{1+BH}{3}\left[2SH\nabla^2H-S\left(\vec{\nabla}H\right)^2-G(H^2-1)\right]-\Theta, \tag{S2}$$

or in dimensional form,

$$\theta_b-\theta_\infty=\frac{1+\frac{\hbar}{k}h}{3\beta}\left[2\sigma_rh\nabla^2h-\sigma_r\left(\vec{\nabla}h\right)^2-\rho g(h^2-h_0^2)\right]. \tag{S3}$$

To test the validity of the proposed ansatz, we reconstruct a differential equation that yields this solution (S2), and check to what extent it deviates from (S1). Equation (S2) can be recast as

$$\frac{1}{2}\left(\frac{\vartheta_b+\Theta}{1+BH}\right)=\frac{1}{6}\left(2SH\nabla^2H-S\left(\vec{\nabla}H\right)^2-G(H^2-1)\right), \tag{S4}$$

and taking its gradient then yields

$$\frac{1}{2}\vec{\nabla}\left(\frac{\vartheta_b+\Theta}{1+BH}\right)=\frac{1}{3}\left(SH\vec{\nabla}\nabla^2H+S\vec{\nabla}H\nabla^2H-\frac{1}{2}S\vec{\nabla}\left(\vec{\nabla}H\right)^2-GH\vec{\nabla}H\right). \tag{S5}$$

To compare equation (S5) to (S1), we note that equation (S1) can be written as $\vec{\nabla}\cdot\left(H^2\vec{F}\right)=0$, which can be satisfied by

$$\vec{F}=\frac{S}{3}H\vec{\nabla}\nabla^2H-\frac{G}{3}H\vec{\nabla}H-\frac{1}{2}\vec{\nabla}\left(\frac{\vartheta_b+\Theta}{1+BH}\right)=0, \tag{S6}$$

or

$$\frac{1}{2}\vec{\nabla}\left(\frac{\vartheta_b+\Theta}{1+BH}\right)=\frac{S}{3}H\vec{\nabla}\nabla^2H-\frac{G}{3}H\vec{\nabla}H. \tag{S7}$$

Subtracting (S5) from (S7), we are left only with the second and third terms on the RHS of (S11),

$$0=\frac{S}{6}\left[\vec{\nabla}\left(\vec{\nabla}H\right)^2-2\vec{\nabla}H\nabla^2H\right]. \tag{S8}$$

The RHS in (S8) can thus be regarded as the difference between the approximate (ansatz) solution and the exact solution (S1),

$$\vec{\epsilon}=\frac{S}{6}\left[\vec{\nabla}[(\partial_XH)^2+(\partial_YH)^2]-2\vec{\nabla}H\left(\partial_X^2H+\partial_Y^2H\right)\right], \tag{S9}$$

which can be written explicitly in terms of its components as

$$\vec{\epsilon} = \frac{S}{3}[(\partial_Y H \partial_{XY}^2 H - \partial_X H \partial_Y^2 H)\ ,\ (\partial_X H \partial_{XY}^2 H - \partial_Y H\, \partial_X^2 H)] \qquad (S10)$$

The ansatz solution is thus exact when the non-normalized Gaussian curvature of the surface, $K = \partial_X^2 H \partial_Y^2 H - (\partial_{XY}^2 H)^2$, vanishes. For other surfaces, the error would depend on the magnitude of the Gaussian curvature, and we provide a numerical assessment for this error in the following section.

## S.3. Numerical verification of the two-dimensional inverse problem solution

We seek a solution that will satisfy equation (S12),

$$F_x = \frac{S}{3} H \partial_X \nabla^2 H - \frac{G}{3} H \partial_X H - \frac{1}{2} \partial_X \left( \frac{\vartheta_b + \Theta}{1 + BH} \right) = 0, \qquad (S11.a)$$

$$F_y = \frac{S}{3} H \partial_Y \nabla^2 H - \frac{G}{3} H \partial_Y H - \frac{1}{2} \partial_Y \left( \frac{\vartheta_b + \Theta}{1 + BH} \right) = 0. \qquad (S11.b)$$

By defining $\mathrm{T} = \frac{\vartheta_b + \Theta}{1+BH}$, the equations can be expressed as

$$\partial_X \mathrm{T} = \frac{2}{3} H [S \partial_X (\nabla^2 H) - G \partial_X H], \qquad (S12.a)$$

$$\partial_Y \mathrm{T} = \frac{2}{3} H [S \partial_Y (\nabla^2 H) - G \partial_Y H]. \qquad (S12.b)$$

We specify a desired deformation map $H(X, Y)$ and integrate equation (S12.a) numerically in $X$ from 0 to an arbitrary coordinate within the domain, $\xi$. The solution can be thus expressed as

$$\mathrm{T} = A_1(\xi, Y) + A_2(Y), \qquad (S13)$$

where $A_1 = \int_{-\mathcal{L}}^{\xi} \frac{2}{3} H [S \partial_X (\nabla_2^2 H) - G \partial_X H] dX$ is the result of the numerical integration and $A_2(Y)$ is an unknown function. Substituting (S13) into equation (S12.b) yields an equation for A2,

$$\frac{d}{dY} A_2(Y) = \frac{2}{3} H [S \partial_Y (\nabla^2 H) - G \partial_Y H] - \partial_Y A_1(X, Y), \qquad (S14)$$

which we integrate numerically in $Y$ between $-\mathcal{L}$ and an arbitrary coordinate within the domain, $\eta$, to find $A_2$. The temperature field is then given by

$$\vartheta_b = (1 + BH)(A_1 + A_2) - \Theta \qquad (S15)$$

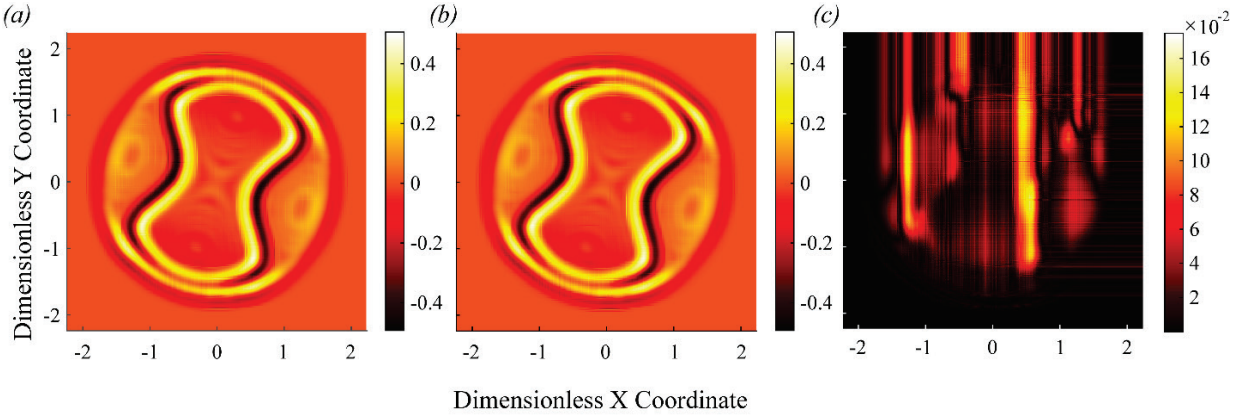


***Figure S4 | A comparison between analytical and numerical solutions to the inverse problem of a tetrapod phase mask.*** *(a) The dimensionless temperature based on the analytical solution S8. (b) The dimensionless temperature based the numerical solution S21. (c) The relative difference (in percent) between the analytical and numerical solutions, showing that the deviation is less than 0.17 %.*

Figure S4 shows a comparison between the resulting dimensionless temperature obtained from the analytical solution (Figure S4a, corresponding to eq. S2) and from the numerical solution (Figure S4b, corresponding to eq. S15) for the case of the 3D localization microscopy mask ('tetrapod mask') presented

in Figure 5 of the main manuscript. For clarity of presentation, we subtracted from both solutions the mean temperature of the boundaries, so that the dimensionless temperature outside the mask area is set to zero. We defined the relative difference between the solutions as the absolute difference between them divided by the amplitude of temperature, and present the results in Figure S4c. As can be seen, the maximal relative difference is approximately $0.17\ \%$.

Figure S5 presents the dimensional temperature map obtained for this case, showing that small deviations on the order of 0.2 degrees are sufficient to produce the desired topography.

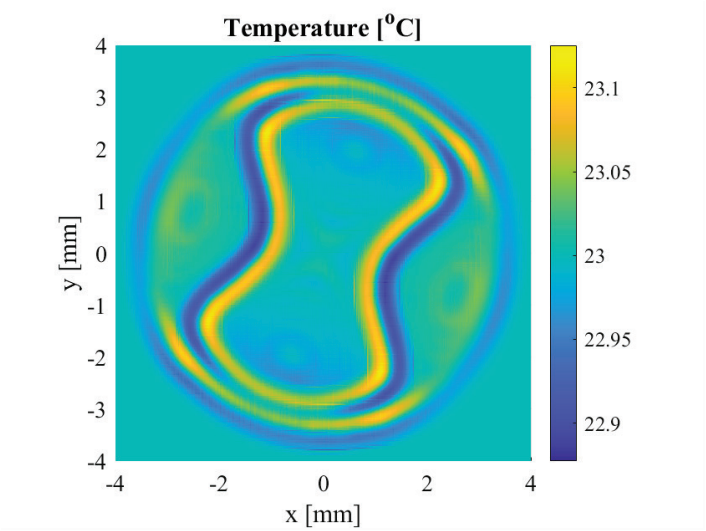


***Figure S5 | The dimensional temperature map corresponding to the saddle-shaped phase mask of Figure 5 in the manuscript.***

## S.4. Material properties

Table S1. Material properties that were used in all of the analytical and numerical solutions.

| Property | Value | Units | Source |
|---|---|---|---|
| $L_x, L_y$ | $6 \cdot 10^{-3}$ | $m$ | Chamber size |
| $h_0$ | $60 \cdot 10^{-6}$ | $m$ | Calculated film thickness based on chamber size and injected volume |
| $\sigma_r$ | 28.5 | $\frac{mN}{m}$ | Based on the properties of the polymer CPS1050 |
| $\beta$ | 0.866 | $\frac{mN}{mK}$ | Based on the properties of the polymer CPS1050 |
| $\rho$ | 1200 | $\frac{kg}{m^3}$ | Based on the properties of NOA63 |
| $\mu$ | 2 | $Pa \cdot s$ | Based on the properties of NOA63 |
| $C_p$ | 1632.852 | $\frac{J}{kgK}$ | Based on the properties of PSF-5cSt oil |
| $k$ | $117.152 \cdot 10^{-3}$ | $\frac{W}{mK}$ | Based on the properties of PSF-5cSt oil |
| $g$ | 9.81 | $\frac{m}{s^2}$ | Earth's gravity acceleration |
| $\hbar$ | 10 | $\frac{W}{m^2K}$ | Estimation based on common natural convection coefficients |
| $\theta_{b_{min}}, \theta_{b_{max}}$ | 23, 25 | $°C$ | Assumed. Used for scaling only. |
| $\overline{\theta_b}$ | 24 | $°C$ | Assumed. Used for scaling only. |
| $\theta_\infty$ | 23 | $°C$ | Assumed. Used for scaling only. |
| $l$ | $2 \cdot 10^{-3}$ | $m$ | Assumed. Used for scaling only. |
| $\nu = \frac{\mu}{\rho}$ | $1.7 \cdot 10^{-3}$ | $\frac{m^2}{s}$ | Calculated |
| $\alpha = \frac{k}{\rho C_p}$ | $5.979 \cdot 10^{-8}$ | $\frac{m^2}{s}$ | Calculated |
| $\Delta\theta = \theta_{b_{max}} - \theta_{b_{min}}$ | 2 | $°C$ | Calculated |

## Appendix A: Derivation of the steady-state equation for the shape of a thin liquid film subjected to a non-uniform temperature distribution

We follow the derivation first presented by Vanhook et. al [2] and derive a 2D steady state equation for the free surface of a liquid film under the action of the thermocapillary effect. As illustrated in Figure S5, we consider a liquid with density $\rho$, dynamic viscosity $\mu$, surface tension $\sigma$, thermal conductivity $k$, and heat capacity $C_p$, filling a shallow square-shaped cavity of length $L$, to an initial height $h_0$.

A small subarea of the substrate with a characteristic length $l$ is heated with a prescribed temperature $\theta_b(x,y)$, which is conducted to the free surface, yielding a non-uniform surface temperature. This yields surface tension gradients, which in turn lead to the transfer of mass along the interface, known as the thermocapillary effect [3]. Throughout the analysis we assume that the film thickness $\mathrm{h}_0$ is significantly smaller than the characteristic length $l$, so that $\varepsilon = \frac{h_0}{l} \ll 1$.

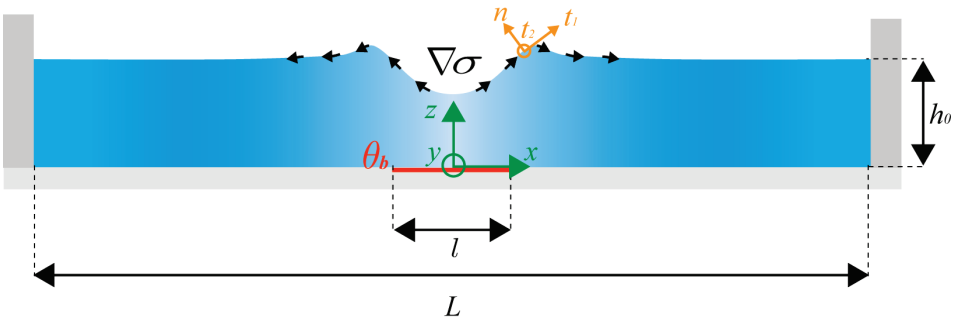


***Figure S5 | Schematic description of the problem under consideration**. A thin liquid film with an initial height $h_0$, rests in a shallow, square-shaped cavity with a side length $L$. A small subarea of the substrate with a characteristic length $l$ is heated with a prescribed temperature $\theta_b(x,y)$. The resulting non-uniform temperature distribution at the free surface induces gradients in surface tension, which, through the thermocapillary effect, lead to deformations of the liquid film.*

### Governing equations and boundary conditions in dimensional form

We separate our problem into a hydrodynamic problem and a thermal one, and begin with the prior. The governing equations are the continuity equation and steady-state Navier-Stokes (NS) equations,

$$\rho(\boldsymbol{\nabla}\cdot\mathbf{U}) = 0, \qquad (A1.a)$$

$$\rho\boldsymbol{U}\cdot\vec{\nabla}\boldsymbol{U} = -\vec{\nabla}p + \mu\nabla^2\boldsymbol{U} + \rho\boldsymbol{g}, \qquad (A1.b)$$

where $\boldsymbol{U}$ is the three-dimensional velocity field, $\boldsymbol{g} = (0,0,-g)$ is the gravity acceleration vector, and $p$ is the pressure.

At $z = 0$ the liquid is subject to no-slip and no-penetration conditions,

$$\boldsymbol{U}(z=0) = 0. \qquad (A2)$$

At the liquid-air interface, $z = h(x,y)$, the normal component of the velocity satisfies the kinematic boundary condition

$$w = \boldsymbol{u_2}\cdot\nabla h\,, \qquad (A3.a)$$

where $h = h(x,y)$ is the position of the free surface, $\boldsymbol{u_2} = (u,v)$ is the planar velocity vector, $\nabla = (\partial_x, \partial_y)$ is the 2D gradient in the $x$ and $y$ directions, and $w$ is the velocity component in the $z$ direction.

Another boundary condition is a stress balance at the free surface,

$$\left(\overline{\boldsymbol{T}} - \overline{\boldsymbol{T}}_{\boldsymbol{air}}\right) \cdot \boldsymbol{n} = 2\mathcal{H}\sigma\boldsymbol{n} + \partial_{t_1}\sigma \cdot \boldsymbol{t_1} + \partial_{t_2}\sigma \cdot \boldsymbol{t_2}. \qquad (A3.b)$$

Here $\partial_{t_i}$ is the directional derivative in the $t_i$ direction ($i = 1,2$), $\overline{\boldsymbol{T}}$ and $\overline{\boldsymbol{T}}_{\boldsymbol{air}}$ are the stress tensors in the liquid and air, respectively, $\boldsymbol{n}$ and $\boldsymbol{t_i}$ are the normal and tangential unit vectors, and $2\mathcal{H}$ is the mean curvature.

## Scaling and asymptotics

We assume that the velocities in the $x, y$ directions are of similar magnitude, and introduce the following scaling

$$\begin{gathered} U = \frac{u}{U_0}, V = \frac{v}{U_0}, W = \frac{w}{W_0}, X = \frac{x}{l}, Y = \frac{y}{l}, Z = \frac{z}{h_0}, \\ H = \frac{h}{h_0}, P = \frac{p}{P_0}, G = \frac{\rho h_0}{P_0} g, \Sigma = \frac{\sigma}{\Delta\sigma}, \end{gathered} \qquad (A4)$$

where $\Delta\sigma$ is a characteristic change in the surface tension resulting from temperature gradients, $\Delta\sigma = \beta\Delta\theta$. The dimensionless governing equations are hence:

$$\varepsilon U_0 \partial_X U + \varepsilon U_0 \partial_Y V + W_0 \partial_Z W = 0, \qquad (A5.a)$$

$$\varepsilon \mathrm{Re}\left(U\partial_X U + V\partial_Y U + \frac{W_0}{U_0\varepsilon} W\partial_z U\right) = -\varepsilon\frac{h_0 P_0}{U_0\mu}\partial_X P + (\varepsilon^2\partial_X^2 U + \varepsilon^2\partial_Y^2 U + \partial_Z^2 U),$$

$$\varepsilon \mathrm{Re}\left(U\partial_X V + V\partial_Y V + \frac{W_0}{U_0\varepsilon} W\partial_z V\right) = -\varepsilon\frac{h_0 P_0}{U_0\mu}\partial_Y P + (\varepsilon^2\partial_X^2 V + \varepsilon^2\partial_Y^2 V + \partial_Z^2 V), \qquad (A5.b)$$

$$\varepsilon \mathrm{Re}\frac{W_0}{U_0}\left(U\partial_X W + V\partial_Y W + \frac{W_0}{U_0\varepsilon} W\partial_z W\right) = -\frac{h_0 P_0}{U_0\mu}\partial_Z P + \frac{W_0}{U_0}\left(\varepsilon^2\partial_X^2 W + \varepsilon^2\partial_Y^2 W + \partial_Z^2 W\right) - \frac{h_0 P_0}{U_0\mu} G,$$

where $\mathrm{Re} = \frac{\rho U_0 h_0}{\mu}$ is the Reynolds number and $U_0$ will be defined in the following section. From the continuity equation (A5.a) we obtain the proper scaling for the velocity in the $z$ direction, $W_0 = \varepsilon U_0$ and from the momentum equations (A5.b) we obtain the proper scaling for the pressure, $P_0 = \frac{\mu U_0}{\varepsilon h_0}$.

Projecting boundary condition (A3.b) onto the first tangential vector $\boldsymbol{t_1}$ yields the equation

$$\varepsilon P_0(\partial_Y H\partial_Z U - \partial_X H\partial_Z V) = \frac{\Delta\sigma}{l}(\partial_X\Sigma\partial_Y H - \partial_Y\Sigma\partial_X H). \qquad (A6)$$

A similar result is achieved by projecting (A3.b) onto the second tangential vector, $\boldsymbol{t_2}$. We substitute the definition of $P_0$ and rewrite (A6) as

$$\partial_Y H\left(\partial_Z U - \frac{\varepsilon\Delta\sigma}{\mu U_0}\partial_X\Sigma\right) - \partial_X H\left(\partial_Z V - \frac{\varepsilon\Delta\sigma}{\mu U_0}\partial_Y\Sigma\right) = 0. \qquad (A7)$$

Since we require the balance in (A7) to hold independently of the derivatives of $H$, we obtain the proper scaling for the velocity, $U_0 = \varepsilon\,\Delta\sigma/\mu$ and the dimensionless boundary conditions (A11.c).

In the normal direction, equation (A3.b) balances the external pressure with the surface tension. We assume that the overall change in surface tension, $\Delta\sigma$, is small relative to a reference surface tension $\sigma_r$

and will further discuss this in the thermal section. Considering the aforementioned assumption, we can write the surface tension as $\sigma \approx \sigma_r$ and by projecting boundary condition (A3.b) onto the normal vector $\boldsymbol{n}$, the normal stress balance condition in dimensionless form can be expressed as

$$-P_0 P = \frac{\varepsilon \sigma_r}{l}(\partial_X^2 H + \partial_Y^2 H). \tag{A8}$$

Substituting the expression for $P_0$ we can rewrite equation (A8) as

$$-P = S(\partial_X^2 H + \partial_Y^2 H), \tag{A9}$$

where $S = \varepsilon^3 \frac{\sigma_r}{\mu U_0} = \varepsilon^2 \frac{\sigma_r}{\Delta\sigma}$ is the surface tension number. For our case $\frac{\sigma_r}{\Delta\sigma} = 10^2 \sim 10^3$ and $\varepsilon^2 = O(10^{-3})$ therefore $S = O(1)$ and the balance is maintained.

With the obtained scaling, we now turn to asymptotic analysis of the NS equations (A5.b). Noting that for the typical values in our system $Re \ll 1$, the leading order of the equations take the form

$$\partial_Z^2 U = \partial_X P, \qquad \partial_Z^2 V = \partial_Y P, \tag{A10.a}$$

$$\partial_Z P = -G, \tag{A10.b}$$

with the boundary conditions at $Z = 0$:

$$U = V = W = 0 \tag{A11}$$

and at $Z = H$:

$$W = U\partial_X H + V\partial_Y H, \tag{A12.a}$$

$$\partial_Z U = \partial_X \Sigma, \qquad \partial_Z V = \partial_Y \Sigma, \tag{A12.b}$$

$$-P = S[\partial_X^2 H + \partial_Y^2 H]. \tag{A12.c}$$

Integrating the continuity equation (A5.a) in the Z direction, applying Leibniz's rule and using the boundary conditions (A11) and (A12.a) we obtain an integral form of the kinematic condition

$$\partial_X \int_0^H U dZ + \partial_Y \int_0^H V dZ = 0. \tag{A13}$$

Solving for the velocity field as a function of the pressure gradient (equations (A10.a) with B.C.s (A11) and (A12.b)), plugging it into equation (A13), and performing the integration yields

$$\left[\partial_X\left(-\frac{\partial_X P H^3}{3} + \frac{\partial_X \Sigma H^2}{2}\right) + \partial_Y\left(-\frac{\partial_Y P H^3}{3} + \frac{\partial_Y \Sigma H^2}{2}\right)\right]_{Z=H} = 0. \tag{A14}$$

Equation (A14) can be compactly written as

$$\boldsymbol{\nabla} \cdot \left[\frac{H^2}{2}\vec{\nabla}\Sigma - \frac{H^3}{3}\vec{\nabla}P\right] = 0, \tag{A15}$$

where $\vec{\nabla} = (\partial_X, \partial_Y)$.

Integrating equation (A10.b) with B.C. (A12.c) allows us to express the pressure gradient in terms of the dimensionless free surface,

$$\vec{\nabla}P = G\vec{\nabla}H - S\vec{\nabla}\cdot\nabla^2 H. \qquad (A16)$$

Substituting (A16) into (A15) results in the final form of the equation for the steady-state position of the free surface,

$$\boldsymbol{\nabla}\cdot\left[\frac{H^2}{2}\vec{\nabla}\Sigma - \frac{H^3}{3}(G\vec{\nabla}H - S\vec{\nabla}\cdot\nabla^2 H)\right] = 0. \qquad (A17)$$

## Thermocapillary effect

In order to evaluate $\vec{\nabla}\Sigma$ we proceed to solve the coupled thermal problem, which is governed by the steady state energy equation,

$$\boldsymbol{U}\cdot\vec{\nabla}\theta = \alpha\left(\partial_x^2\theta + \partial_y^2\theta + \partial_z^2\theta\right), \qquad (A18)$$

where $\theta$ is the liquid's temperature and $\alpha = \frac{k}{\rho C_p}$ is its thermal diffusivity.

At $z = 0$ the liquid is subject to a prescribed temperature profile $\theta_b(x, y)$:

$$\theta(z = 0) = \theta_b(x, y), \qquad (A19)$$

and the heat transfer at the liquid-air interface, $z = h(x, y)$, is described by Newton's cooling law:

$$k\vec{\nabla}\theta_h\cdot\boldsymbol{n} + \hbar(\theta_h - \theta_\infty) = 0, \qquad (A20)$$

where $\hbar$ is the heat transfer coefficient and $\theta_\infty$ is the ambient gas temperature.

We scale the temperature by $\vartheta = \frac{\theta - \overline{\theta}_b}{\Delta\theta}$, where $\Delta\theta = \theta_{b_{max}} - \theta_{b_{min}}$, and $\overline{\theta}_b$, $\theta_{b_{max}}$, $\theta_{b_{min}}$ are the average temperature at the base, and its maximum and minimum values, respectively.

Equation (A18) in dimensionless form is thus

$$\varepsilon\mathrm{Pe}(U\partial_X\vartheta + V\partial_Y\vartheta + W\partial_Z\vartheta) = \varepsilon^2\partial_X^2\vartheta + \varepsilon^2\partial_Y^2\vartheta + \partial_Z^2\vartheta, \qquad (A21)$$

where $\mathrm{Pe} = \frac{U_0 h_0}{\alpha}$ is the thermal Peclet number. We note that in our case $\mathrm{Pe} = \frac{\varepsilon\Delta\sigma h_0}{\alpha\mu} = O(10^{-3}) \ll 1$.
We proceed to write $\vartheta$ as an asymptotic expansion in $\varepsilon$, which at the leading order yields

$$\partial_Z^2\vartheta = 0, \qquad (A22)$$

with the boundary conditions

$$\begin{aligned} Z = 0: &\qquad \vartheta_b = \frac{\theta_b - \overline{\theta}_b}{\Delta\theta}, \\ Z = H(X, Y): &\qquad [\partial_Z\vartheta + B(\vartheta + \Theta)]_{Z=H} = 0, \end{aligned} \qquad (A23)$$

where $\vartheta_b$ is the dimensionless temperature distributions at the bottom surface, $\Theta = \frac{\overline{\theta}_b - \theta_\infty}{\Delta\theta}$ is a ratio between temperature differences, and $B = \frac{\hbar h_0}{k}$ is the Biot number.

Equation (A22) with B.C.s (A23) yields the temperature distribution inside the liquid film

$$\vartheta = \vartheta_b - \frac{(\vartheta_b + \Theta)B}{1 + BH} Z, \tag{A24}$$

and hence $\vartheta|_{Z=H} = \frac{\vartheta_b - BH\Theta}{1+BH}$.

We assume that the surface depends solely on the temperature at the interface $\sigma = \sigma\big(\theta(x, y, z = h)\big)$, and that for small variations in temperature the surface tension changes linearly such that

$$\Delta\sigma = -\beta\Delta\theta_{z=h}, \tag{A25}$$

where $\beta$ is a positive constant and a property of the material and $\Delta\theta_{z=h}$ is the variation in temperature at the interface. The negative sign on the RHS of (A25) represents a decrease in surface tension as the temperature increases. This is consistent with our previous assumption of small variations in surface tension since for the liquid we used $\frac{\beta}{\sigma_r} \approx 10^{-3}\frac{1}{^\circ K}$ and for our system $\Delta\theta_h \approx 1^\circ K$.

Using the chain rule, its gradient can be written as:

$$\vec{\nabla}\sigma = \frac{d\sigma}{d\theta}\big(\vec{\nabla}\theta_{z=h} + \Delta\theta\partial_z\theta_{z=h}\vec{\nabla}h\big). \tag{A26}$$

In dimensionless form the surface tension gradient is

$$\vec{\nabla}\Sigma = -\big(\vec{\nabla}\vartheta_{Z=H} + \partial_Z\vartheta_{Z=H}\vec{\nabla}H\big), \tag{A27}$$

Substituting equation (A24) into (A27) we obtain

$$\vec{\nabla}\Sigma = -\vec{\nabla}\left(\frac{\vartheta_b + \Theta}{1 + BH}\right). \tag{A28}$$

Further substituting equation (A28) into equation (A17) yields the final equation defining the relation between the prescribed temperature and the resulting surface topography:

$$\boldsymbol{\nabla}\cdot\left[\frac{S}{3}H^3\vec{\nabla}\nabla^2 H - \frac{G}{3}H^3\vec{\nabla}H - \frac{1}{2}H^2\vec{\nabla}\left(\frac{\vartheta_b + \Theta}{1 + BH}\right)\right] = 0. \tag{A29}$$

## References


[1] E. Cuche, P. Marquet, and C. Depeursinge, Simultaneous Amplitude-Contrast and Quantitative Phase-Contrast Microscopy by Numerical Reconstruction of Fresnel off-Axis Holograms, Applied Optics **38**, 6994 (1999).

[2] S. J. Vanhook, M. F. Schatz, J. B. Swift, W. D. Mccormick, and H. L. Swinney, Long-Wavelength Surface-Tension-Driven Bénard Convection: Experiment and Theory, J. Fluid Mech. **345**, 45 (1997).

[3] M. Tan, S. Bankoff, and S. H. Davis, Steady Thermocapillary Flows of Thin Liquid Layers. I. Theory, Physics of Fluids A: Fluid Dynamics **2**, 313 (1990).